Journal of Constructional Steel Research 241 (2026) 110290

Contents lists available at ScienceDirect

Journal of Constructional Steel Research

journal homepage: www.elsevier.com/locate/jcsr

Shape optimisation of metal additive manufacturing connections in lightweight steel structures

Chuandong Xie [a,*], Alireza Bagheri Sabbagh [a], Ehsan Bakhshivand [a], Ornella Iuorio [b]

[a] School of Engineering, University of Aberdeen, Aberdeen, AB24 3FX, UK
[b] Department of Architecture, Built Environment and Construction, Politecnico di Milano, Milan, 20133, Italy

ARTICLE INFO

Keywords:
Metal additive manufacturing
Optimisation
Lightweight steel framing
Explainable AI

ABSTRACT

The application of metal additive manufacturing (AM) to connections in lightweight side framing structure is explored. Two connection concepts are considered, namely key-wheel (KW) and gear-wheel (GW) connections. To identify the optimal wheel geometries for the proposed KW and GW connections, a genetic algorithm with multiple-objectives optimisation framework was employed. The optimised parameters included wheel radius R, tooth number n, along with other geometrical wheel parameters. The optimisation objectives were to maximise the initial rotational stiffness, yield strength and peak strength directly for the connections with Laser Metal Deposition (LMD) process, while an additional constraint of normalising these objectives with respect to material use was introduced for the connection with Wire Arc Additive Manufacturing (WAAM) process. The optimisation results suggest a wheel shape with 12 elongated teeth for the KW connection, and a shallow-tooth wheel shape for the GW connection. The maximum joist deflections of the frame-level analysis are reduced by 14%–20% when employing the optimised connections, while the normalised initial stiffness, yield strength and peak strength are increased by 69.6%–101.2%, 58.7%–212.6%, 48.8%–164.7%, respectively. In general, GW connection exhibits greater level of mechanical properties compared to the KW connection, while both connections offer viable alternatives since each of them showed trade-offs depending on performance requirements and practicality.

1. Introduction

Lightweight steel framing (LSF) structures using cold-formed steel (CFS) have been shown to be highly effective in reducing steel consumption [1,2]. Traditional practices include platform framing, balloon framing and ledger framing [3], each typically implemented using either a sequential construction method (SCM) or continuous construction method (CCM) [4]. Although ledger framing has become prevalent because of its applicability in multi-storey systems, the joist-to-stud connections that are considered as shear-only resistance lead to relatively heavy flooring joist designs and local failure limit states within the connection components [3]. Alternatively, a side frame LSF system developed by Sabbagh and Torabian [5] employs in-plane semi-rigid floor-to-wall screwed connections, which can reduce the joist's mid-span deflection and eliminate the local failure limit states. However, the shear/pull-out failure at the corner screws may lead to a relatively sharp strength degradation and potentially a premature failure limit state due to the non-even distribution of the screw forces.

Metal additive manufacturing (AM) has emerged as an impactful tool to shift the manufacturing paradigm as it provides a manufacturing idea of adding, which is different from conventional manufacturing techniques [6–10]. By constructing components layer-by-layer from three-dimensional (3D) model data using automated processes [11,12], metal AM enables the possibility of creating complex-shaped 3D parts that are difficult or impossible to obtain using traditional processes and reducing material consumption and waste [13,14]. Significant progress has already been achieved in applying this technique across various engineering disciplines, e.g., aerospace [15], space [16], biomedical [17], mechanical [18], automotive [19] and shipbuilding [20] engineering. In recent, by combining metal AM and conventional manufacturing (CM), a hybrid manufacturing concept has emerged [21–23], with the applications on structural member strengthening [24–27], connections [28–31] and fatigue strengthening of damaged members [32,33], among others. For instance, in the three-point bending tests on I-section beams conducted by Yang et al. [27], an approximately 11.5% increase in mass due to the strengthening by Wire Arc Additive Manufacturing (WAAM) yield up to 25.8% and 22.4% increases in ultimate bending moment resistance and initial stiffness, respectively. Overall, this

* Corresponding author.
E-mail address: chuandong.xie@abdn.ac.uk (C. Xie).

https://doi.org/10.1016/j.jcsr.2026.110290
Received 28 September 2025; Received in revised form 19 December 2025; Accepted 5 February 2026
Available online 14 February 2026

hybrid concept can reduce the environmental impact associated with large-scale adoption of metal AM in construction.

To address the technical and practical limitations of traditional joist-stud connections, a key-wheel (KW) and a gear-wheel (GW) connections have been developed, considering two prevalent metal AM methods including laser metal deposition (LMD) and WAAM [34]. The proposed connections provide a fastener-free type of connection method as an alternative for the traditional and labour-intensive types of connections for the joist-stud framing installation. However, variations in wheel geometry can significantly influence the moment-resisting performance in both elastic and inelastic stages.

To identify the optimal wheel geometries for the proposed KW and GW connections, this study employed a multi-objective optimisation framework based on a genetic algorithm. Genetic algorithm has been considered as an effective approach for solving both constrained and unconstrained optimisation problems by mimicking biological evolution progresses [35,36], and has been widely applied in various fields, including seismic engineering [37,38] and LSF design [39–42]. The optimisation aimed to maximise the initial rotational stiffness, yield strength and peak strength directly for the connections with LMD process, while an additional constraint of normalising these objectives by material use was introduced for the connections with WAAM process, in order to reduce heat input and distortion to the substrate. Additionally, Explainable Artificial Intelligence (AI) technique [43–46] were also employed to investigate the inherent trade-off behaviour among the competing objectives and highlight the feature importance. Finally, structural level evaluations were conducted to compare the gravity-only and gravity combined with lateral force loading responses of the frames implementing original versus optimised connections.

2. AM-CFS connections

2.1. Configurations and AM processes

Fig. 1 shows the proposed additive manufacturing connections for lightweight side framing. The KW connection, shown in Fig. 1(a), consists of a wheel shape component with numbers of teeth printed on the stud and a joist matching cut with the same shape. Therefore, the joists can be easily installed on the studs by sliding during construction. The tooth shape enables an interlocking mechanism between joists and studs, creating a semi-rigid moment-resisting connection. The GW connection, shown in Fig. 1(b), provides an alternative that prints a matching wheel component with either smaller or larger shape and minimum gap on the joists, instead of cutting. The female–male wheel pair provides interlocking mechanism for the semi-rigid moment-resisting joist-to-stud connections.

Seven parameters were identified to define the geometry of the wheel shape, including wheel radius R, tooth number n, outer length ratio r_{OL}, inner length ratio r_{IL}, tooth depth ratio r_{TD}, fillet radius of the corners R_f and wheel thickness t. The parameters R, n and r_{TD} primarily determine the standard profile of the wheel, as shown on the left side of Fig. 2. The standard shape can then be generalised by applying the outer and inner length ratio, respectively. The fillet radius R_f modifies the curvature at the corners of the shape, as shown on the right side of Fig. 2. Lastly, the wheel thickness t may also significantly influence the moment-resisting behaviour. By varying these parameters, a wide range of wheel shapes can be generated, each potentially resulting in different interlocking mechanisms and moment-resisting performance.

Both WAAM and LMD processes can be adopted for the proposed AM-CFS connections. In the WAAM process, metal is deposited by melting a continuous wire, which enables a high deposition rate and printing efficiency [47,48]. This makes WAAM a suitable option for large-scale structural application in structural engineering [9,49]. However, the large heat input and extensive melt pool lead to longer cooling time. Components produced by WAAM exhibit relatively high surface roughness and geometric waviness, which necessitate larger assembly clearances. Although surface quality can be improved through post-processing methods such as machining, this may compromise the inherent advantages of WAAM in terms of efficiency and cost. In addition, the higher heat input can lead to more pronounced residual stresses, and penetration defects may occur more readily in thin-walled components [10,50]. In contrast, LMD employs a focused laser to generate a small molten pool and melt metal powder particles [51]. The heat input is highly localised, and the substrate acts as an effective heat sink, resulting in rapid self-cooling immediately after the laser passes [52]. Hence, LMD offer better dimensional control and lower residual stresses [53], allowing smaller assembly clearances to be achieved. As primary research, this study employed both processes and shed lights on the working mechanism with different wheel shapes.

2.2. Idealised moment–rotation relationship

The moment–rotation relationship of the AM-CFS connections can generally be represented by a KW-LMD connection with a wheel shape of R = 65 mm, n = 10, r_{OL} = 0.1, r_{IL} = 1.0, r_{TD} = 0.3, R_f = 3.5 mm, t = 2.0 mm, as shown by the grey curve in Fig. 3, which exhibits an initial elastic stage, a smooth elastic–inelastic transition, a distinct peak strength and subsequent degradation. To effectively capture this behaviour and identify the yield strength, an equivalent energy elastic–plastic (EEEP) method was adopted, based on ASCE 41-23 [54]. First, the peak strength was identified from the current curve. An elastic–perfectly plastic (EPP) curve was then derived using the EEEP method. Based on the rotation corresponding to the yielding point of the EPP curve, the intersection with the actual moment–rotation curve was defined as M_y^0. By connecting the origin to the point corresponding to $0.6M_y^0$ on the actual curve, the initial rotational stiffness was determined. Applying the EEEP method again yielded the final yield moment M_y. This procedure ensures that the idealised moment–rotation curve dissipates the same amount of energy as the actual response up to the peak strength. Post-peak degradation behaviour is more complex. A stiffness degradation ratio α_2 and a strength reduction factor β was suggested, but the appropriate values remain open and require further investigation. Nevertheless, the idealised initial rotational stiffness, yield and peak strengths provide an accurate representation of the connection response up to peak strength. The corresponding function of the idealised curve is shown in Eq. (1).

$$M = \begin{cases} k_e\theta & \theta \le \theta_y \\ M_y + (\theta - \theta_y)\alpha_1 k_e & \theta_y < \theta \le \theta_d \\ M_d + (\theta - \theta_d)\alpha_2 k_e & \theta_d < \theta \le \theta_u \\ \beta M_y & \theta_u < \theta \end{cases} \quad (1)$$

3. Optimisation framework

3.1. Objectives

The idealised moment–rotation relationship highlights three parameters, including initial rotational stiffness k_e, yield strength M_y and peak strength M_u. A higher initial rotational stiffness and yield strength enhance moment resistance during the elastic stage, while a higher peak strength improves the inelastic response. Two metal AM processes were considered, including LMD and WAAM. For the LMD process, the objectives were to maximise initial rotational stiffness k_e, yield strength M_y and peak strength M_u directly, while these parameters were normalised by the volume wheel component to minimise the heat input, for the WAAM process, represented by $\overline{k}_e$, $\overline{M}_y$ and $\overline{M}_u$, respectively. It should be noted that the heat input in the WAAM process is governed by numerous coupled factors, including arc energy input, wire diameter and feed speed, as well as travel path and travel speed, etc [55]. As the WAAM process parameters were kept consistent (presented in Section 3.5), and the focus was on component-level performance, it is reasonable to adopt a first order approximation in which the deposited steel volume is assumed to be linearly proportional to the heat input.

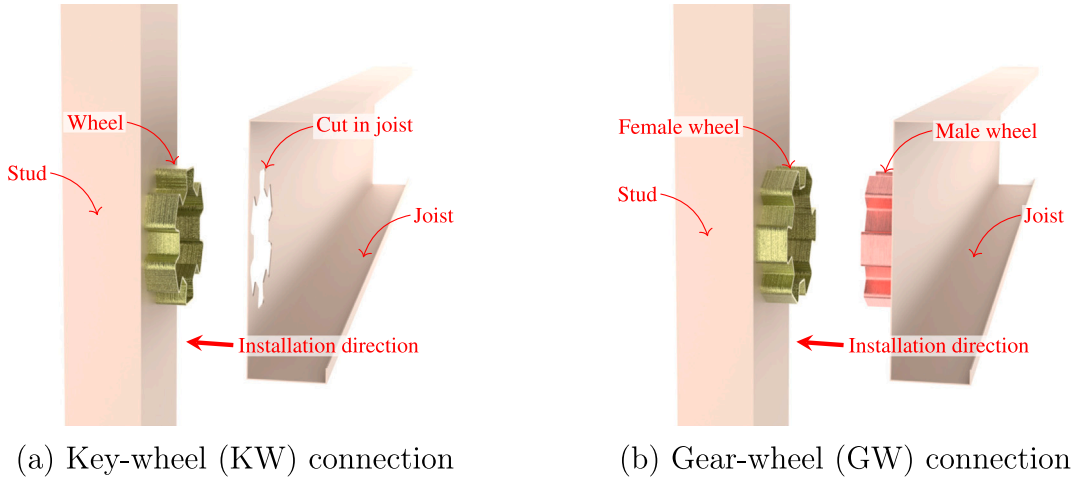

(a) Key-wheel (KW) connection (b) Gear-wheel (GW) connection

Fig. 1. Assembly views of additive manufacturing connections.

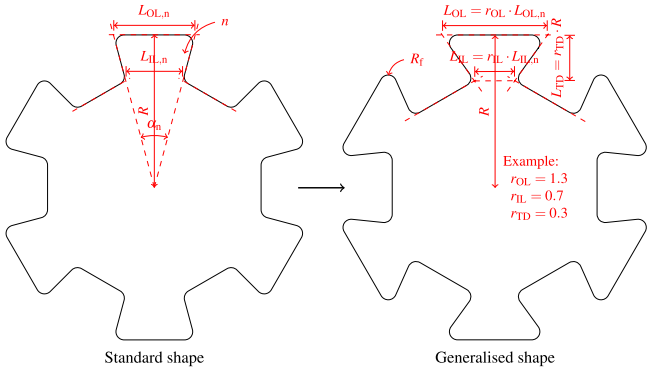

Fig. 2. Wheel shape parameters.

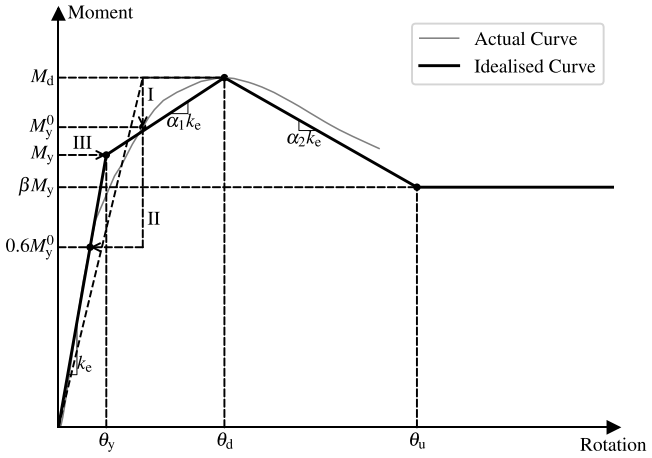

Fig. 3. Idealised moment–rotation relationship.

3.2. Design space

Table 1 shows the ranges of parameters used in the optimisation study. The wheel radius R of 50 mm, 55 mm, 60 mm, 65 mm and tooth number n ranging from 3 to 12 with a step of 1 were considered. The outer length ratio r_{OL} and inner length ratio r_{IL} were both varied from 0.7 to 1.3 with a step of 0.01, and the tooth depth ratio r_{TD} ranged from 0.1 to 0.5 with a step of 0.01. The fillet radius R_f of 0.8 mm, 1.0 mm, 1.5 mm, 2.0 mm, 2.5 mm and 3.0 mm and wheel thickness t from 2.0 mm to 5.0 mm with a step of 0.5 mm were adopted.

Table 1
Parameter ranges.

Parameters	Values
R	50.0 mm, 55.0 mm, 60.0 mm, 65.0 mm
n	3 to 12 with a step of 1
r_{OL}	0.7 to 1.3 with a step of 0.01
r_{IL}	0.7 to 1.3 with a step of 0.01
r_{TD}	0.1 to 0.5 with a step 0f 0.01
R_f	0.8 mm, 1.0 mm, 1.5 mm, 2.0 mm, 2.5 mm and 3.0 mm
t	2.0 mm to 5.0 mm with a step of 0.5 mm

3.3. Genetic algorithm implementation

Genetic algorithm (GA) was adopted for this multiple-objective optimisation procedure, implemented using the evolutionary computation framework — Distributed Evolutionary Algorithms in Python (DEAP) [56]. To facilitate the modelling of wheel components, the open-source parametric 3d modeller FreeCAD [57] was employed. The connection responses were obtained through the numerical analysis in Abaqus [58]. The objectives were then calculated based the idealised moment–rotation curve (Eq. (1)). Therefore, the optimisation process was executed in Python [59], interfacing with both FreeCAD and Abaqus. The population size and number of generations were both set to 150, ensuring a comprehensive exploration of the design space. The NSGA-III algorithm was employed to perform Pareto-front selection, where the Pareto front refers to the set of solutions that are non-dominated with respect to each other and represent trade-offs among multiple objectives [60]. Fig. 4 shows the analysis steps as explained below.

Step 1: Randomly generate the first generation based on the parameter space defined in Table 1.

Step 2: Use FreeCAD to create IGES files containing the wheel geometry for each individual based on its parameters.

Step 3: Create Abaqus models based on the IGES files and submit them for analysis.

Step 4: Evaluation the fitness of each individual based on the objectives using the idealised moment–rotation relationship.

Step 5: Perform Pareto-based selection using the NSGA-III algorithm [60].

Step 6: Apply crossover to the selected individuals with the independent probability of 0.5.

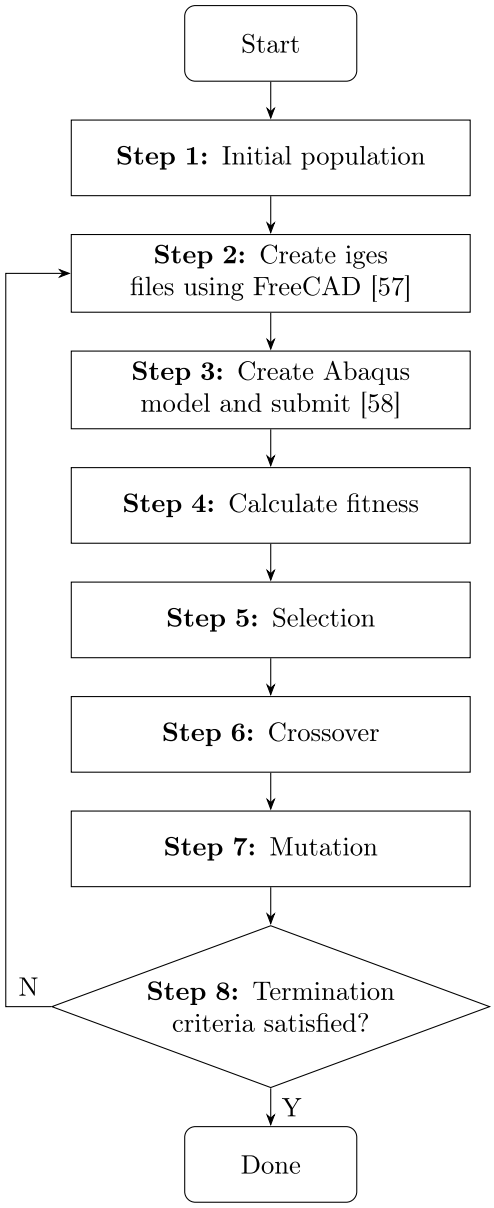

Fig. 4. GA flowchart.

Step 7: Apply mutation to the offspring with the independent probability of 0.2.

Step 8: Check the termination criteria (150 generations). If the criteria are not met, return to Step 2 using the new generation of parameters.

3.4. Finite element method

The connection finite element (FE) modelling is shown in Fig. 5. CFS channel sections of 150M14-75 and 240M13-75 with 15 mm lips were used for studs and joists, respectively. In the section labels, the leading number denoted the section depth in millimetres, followed by the section thickness in 0.1 millimetres after the letter "M", and ending with the flange width in millimetres.

S450 steel, as specified in Eurocode [61], was used for the stud and joist, and its full stress–strain behaviour was modelled based on the formulation proposed Gardner and Yun [62]. For the wheel components fabricated using LMD process, the constitutive model developed by Hradil et al. [63] was adopted, calibrated against tensile coupon tests conducted by Cacace et al. [64]. The WAAM wheel components were modelled using the normal-strength steel constitutive model proposed by Huang et al. [65]. The orthotropic elastic and plastic material properties were represented using the *LAMINA and *POTENTIONAL keywords, respectively [66]. All structural components were modelled using S4R shell elements. A global mesh size of 10 mm was applied to all CFS members, except for the ends of joists, where a refined mesh size of 1 mm was used. The simulations used a general static solver with artificial stabilisation. Since the objectives were normalised, small clearance between the wheel and joist cut, or between the female and male wheels would not affect the final optimisation results. Therefore, these gaps were neglected, which also accelerated the optimisation process and reduced computational cost. Contact interactions between all parts including joist-to-stud, joist-to-wheel, female-to-male wheel components in GW connection were defined using *CONTACT PAIR algorithm with finite sliding in Abaqus [58]. Tangential contact behaviour was defined using a penalty formulation with a friction coefficient of 0.2 and a contact stiffness of 5.8 kN/mm. Normal contact behaviour was modelled using "Hard" contact with a nonlinear penalty formulation. Enhanced translational restraint in the x-direction was applied to the joist to isolate the joist-wheel interaction. Geometric imperfections were implemented to provide a first-order representation of distortion induced by residual stresses and manufacturing deviations in this structural-level assessment [49]. A displacement-controlled vertical load was applied at the joist end, with a target of either a minimum of 80% post-peak degradation or rotation drift of 0.04 rad, whichever occurred first. All moment responses were normalised by the bending capacity of the joist section.

3.5. Validation on FE method

(1) Validation against ledger-framed connection tests

To ensure the key mechanical behaviour of the CFS frames are effectively captured, results from the ledger-framed connection test conducted by Ayhan and Schafer [3] were used. Two main configurations of the ledger-framed tests were selected, labelled by T4 and T5 [3], where the joist is positioned at the midpoint of stud spacing and near a stud, respectively. All modelling methodologies and details, including element type and size, contact behaviour, connection fasteners, and analysis algorithm, are identical to the models adopted herein. The only difference is the pull-out behaviour of steel-to-steel connections, for which the results of the experimental study by Castaneda and Peterman [4] were incorporated. Figs. 6 and 7 show the obtained results based on the developed FE modelling for T4 and T5 tests. As can be seen, both the predicted failure modes and the moment–rotation responses reasonably agree with those of the corresponding experimental tests.

(2) Validation against AM-CFS connection tests

The FE method was further validated against cyclic tests of the KW-WAAM and GW-LMD connections conducted by the authors, using the updated material properties. The wheel radii (measured from the geometric centre to the outer edge) for the KW and GW connection are 55.8 mm and 56.2 mm, respectively. All other geometric parameters are the same, with a tooth number of 4, inner and outer length ratios of 1.0, a tooth depth ratio of 0.3, a fillet radius of 3.0 mm and a wheel depth of 30.0 mm. The KW and GW connections were manufactured using WAAM and LMD processes, respectively, with the thicknesses of the printed components of 3.3 mm and 1.1 mm, respectively. Clearances of 0.7 mm and 0.3 mm were considered between the wheel and joist cut in the KW-WAAM connection and between the female and male wheels in the GW-LMD connection, respectively. The corresponding printing parameters for WAAM and LMD are summarised in Tables 2 and 3, respectively. It was found that the thermal input from WAAM printing has negligible effects on the CFS material properties, evidenced by the coupon test results for the locations shown in Fig. 8. The thermal

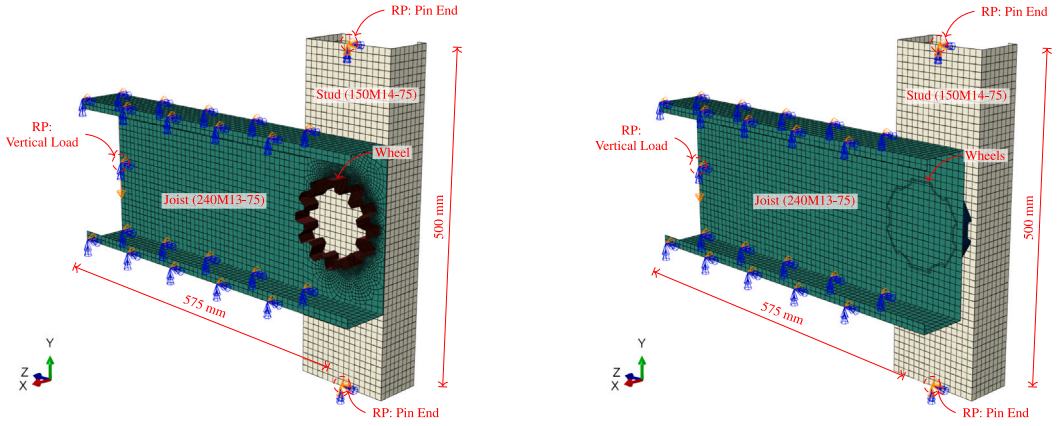

(a) KW connection (b) GW connection

Fig. 5. FE model of connections.

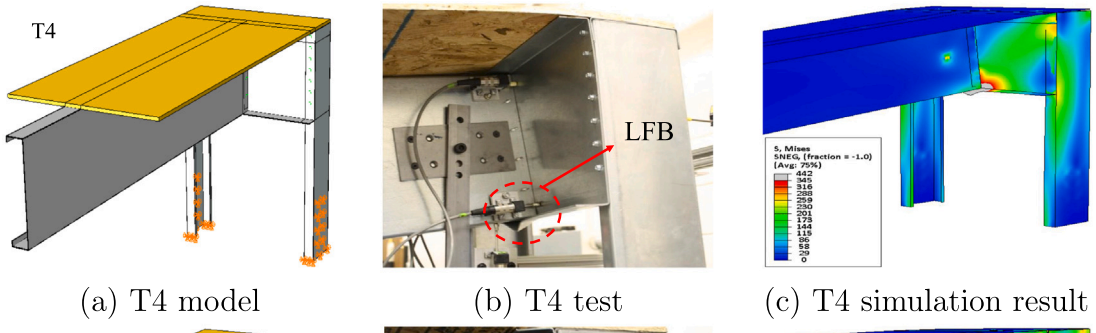

(a) T4 model (b) T4 test (c) T4 simulation result

(d) T5 model (e) T5 test (f) T5 simulation result

Fig. 6. Validation against ledger-framed connection tests.

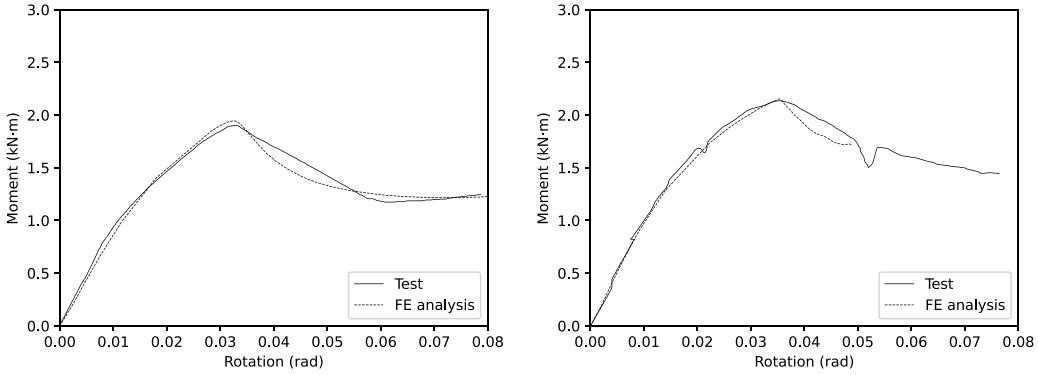

(a) T4 (b) T5

Fig. 7. Comparisons of ledger-framed connection tests.

Table 2
WAAM process parameters.

Para-meters	Wire feed rate (m/min)	Travel speed (mm/s)	Welding voltage (V)	Welding current (A)	Gas flow rate (L/min)	Welding mode	Shielding gas	Dwell time (min)	Layer height (mm)
Values	1.5	5.5	9.7	58	15	MIG CMT	98% Ar + 2% CO_2	2.0(2.5) (3.0)	1.9

Table 3
LMD process parameters.

Para-meters	Powder flow rate (gr./min)	Travel speed (mm/s)	Laser power (W)	Stand-off distance (mm)	Laser spot (mm)	Shielding gas flow rate (L/min)	Carrier gas flow rate (L/min)	Shielding gas	Layer height (mm)
Values	8	18	400	8	1.2	15	5	100%Ar	0.3

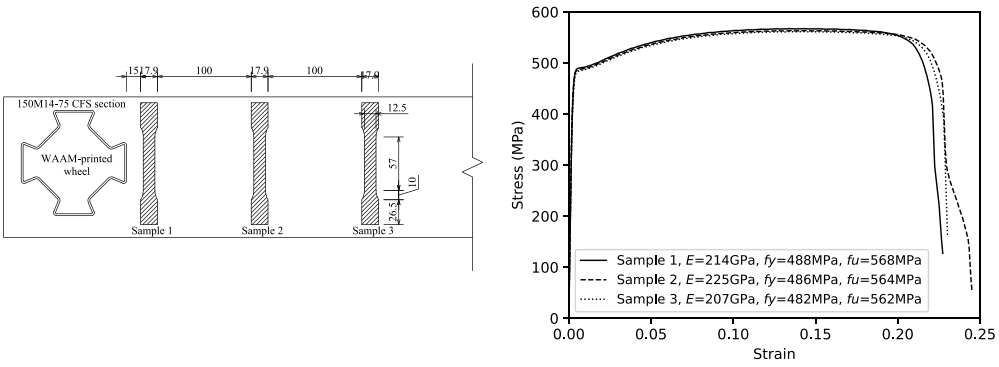

(a) Sample position (b) Stress-strain curves

Fig. 8. CFS coupon test locations and results.

input only increases the yield and ultimate strengths by approximately 1.2%. Therefore, adopting the original CFS material properties, with slightly lower yield strength, is considered appropriate. Distortion due to residual stress effects and manufacturing deviations were accounted for by introducing geometric imperfections [49]. For the CFS components produced by LMD, the thermal input is significantly lower. Consequently, thermal effects were assumed to be negligible. Nevertheless, the thermal effects and residual stresses are sensitive to the printing parameters, substrate geometry, cooling method and fixturing setup, and will therefore be a key focus of future investigations.

Figs. 9 and 10 show the von-Mises stress distribution results and the corresponding hysteretic curves. For the KW-WAAM connections (Fig. 9(a)), high stress concentrations and yielding occurred in the joist web around the printed wheel, while the wheel itself remained elastic which reflects the test observation. For the GW-LMD connections (Fig. 9(b)), limited yielding was observed in both the joist and the printed components. Fig. 10 demonstrates that the proposed FE method can represent the cyclic responses of the AM-CFS connections with reasonable accuracy in terms of the overall trend, the initial rotational stiffness and the peak moments.

4. Optimisation results

4.1. Optimised shapes

Fig. 11 shows the objective values normalised by their maximum values across all generations. All objectives were significantly improved during the first 20 generations. By the 150th generation, all objectives stabilised, indicating convergence of the optimisation process. Fig. 12(a) shows the parallel coordinates plot of the first generation for the KW connection using the LMD process. The left side of the plot displays the shape parameters including wheel radius R, tooth number n, outer length ratio r_{OL}, inner length ratio r_{IL}, tooth depth ratio r_{TD}, fillet radius of the corners R_f and wheel thickness t. In this initial generation, parameter values were randomly assigned for each individual. On the right side, the non-dimensional objective parameters including initial rotational stiffness k_e, yield strength M_y and peak strength M_u are shown.

After 150 generations, the parameter space became more structured, as shown in Fig. 12(b). This generation included both optimised individuals and those generated through crossover and mutation. Notably, the maximum values of the initial rotational stiffness k_e, yield strength M_y and peak strength M_u increased to 36.56, 0.26 and 0.32 (these values are non-dimensional since the original strengths have been normalised by the bending capacity of the joist section), respectively, which were 9.6%, 18.2% and 6.7% higher than the first generation, respectively. However, it is important to note that these objectives cannot be maximised simultaneously, indicating inherent trade-offs among them. Fig. 13 visualises the entire population in 150th generation, with the Pareto fronts highlighted. For both the LMD- and WAAM-based connections, Pareto-optimal individuals lie along the boundary of the objective space, demonstrating higher values of initial rotational stiffness, yielding strength and peak strength. The GW connections tend to achieve even higher objective values compared to KW connections.

Fig. 14 shows the Pareto fronts for both the KW and GW connections with LMD and WAAM processes after 150 generations. The parameter space for the KW connection with LMD process becomes notably clearer, yielding 46 optimised individuals, as shown in Fig. 14(a), compared to Fig. 12(b). The optimisation suggests specific values for the connections: a wheel radius R of 65.0 mm, tooth number n of 12 and outer length ratio r_{OL} of 0.7, resulting in a wheel with 12 teeth. The inner length ratio r_{IL} and the tooth depth ratio r_{TD} are recommended within the ranges of 0.71–1.16 and 0.26–0.49, respectively, yielding an elongated rectangular tooth profile. The fillet radius R_f falls within 0.8–1.5 mm, indicating a preference for sharper corners, and smaller fillet radii provides higher initial rotational stiffness. The thickness t ranges from 2.0 to 4.0 mm, covering most design possibilities, and each value supports either higher initial rotational stiffness or yield

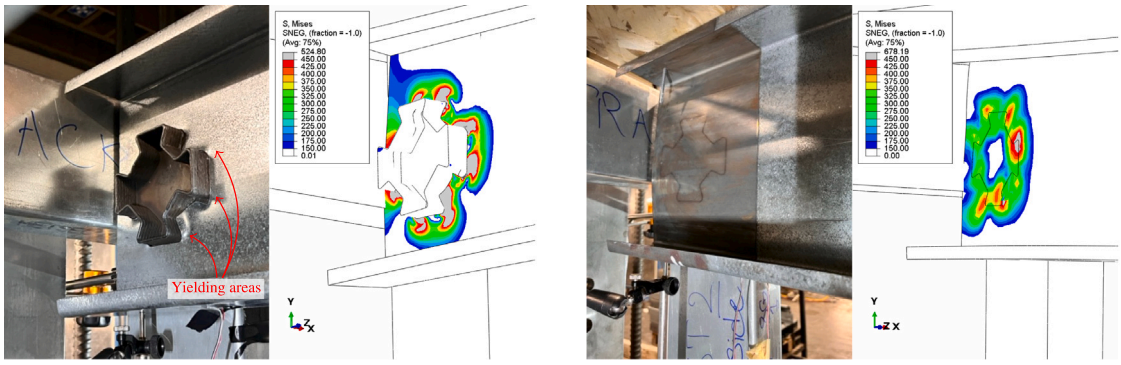

Fig. 9. FE validation against AM-CFS connection tests: tested connection failure modes and FE stress distribution.

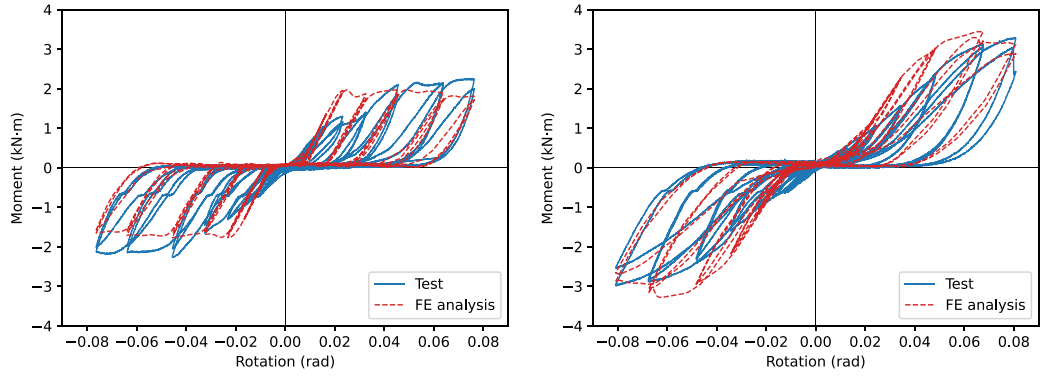

Fig. 10. FE and test cyclic responses of AM-CFS connection tests.

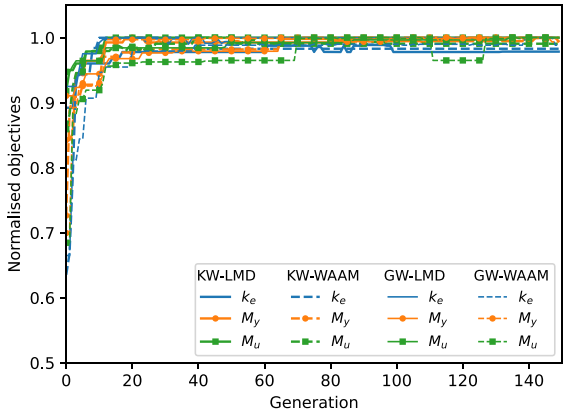

Fig. 11. Normalised objectives across generations.

and peak strengths. The initial rotational stiffness and yield strength exhibit a trade-off, whereas the peak strength and the yield strength are positively correlated.

Fig. 14(b) shows the 24 optimised solutions for the KW connections with WAAM process, where the material usage is limited to reduce heat input and thereby minimise distortion. Similar to the KW-LMD results (Fig. 14(a)), all individuals feature a wheel radius R of 65.0 mm, tooth number n of 12 and smaller outer length ratio r_{OL} around 0.7. However, the inner length ratio r_{IL} and the tooth depth ratio r_{TD} fall within 0.89–1.29 and 0.20–0.28, respectively, suggesting that the teeth remain rectangle though shorter than the KW-LMD connections. The fillet radius R_f ranges from 1.0 to 2.0 mm. Again, sharper corners associated with higher initial rotational stiffness. Due to the material constraint, all individuals adopt the minimum thickness of 2.0 mm. The initial rotational stiffness and yield strength continue to show a trade-off, while the relationship between yield and peak strengths is not patternable. Interpretation of this trade-off behaviour is further discussed in Section 4.2.

Fig. 14(c) shows 24 Pareto-optimal solutions for GW connections with LMD process. Once again, a wheel radius R of 65.0 mm has been adopted by all the optimised results. However, the tooth number drops to 3, and both outer length ratio r_{OL} and inner length ratio r_{IL} increased to values around 1.30. Meanwhile, the tooth depth ratio r_{TD} is suggested with relatively small values around 0.1. This results in a three-side shallow teeth wheel. The fillet radius R_f and the thickness t fall within the range of 0.8–1.5 mm and 3.5–4.5 mm, respectively. In general, individuals with higher initial rotational stiffness exhibit lower yield strength, and vice versa.

For the GW connections with WAAM process, similar results were obtained compared to those of the GW-LMD connections, as shown in Fig. 14(d), except for tooth number n of 4–6, fillet radius R_f of 3.0 mm and the thickness t of 2.0 mm. These modifications aim to reduce the material usage while trying to achieve higher initial rotational stiffness, yield strength and peak strength. Only eight optimised individuals were obtained, and again a clear trade-off was observed among the objectives.

Table 4 summarises all the aforementioned parameters along with two representative examples, where the first example corresponds to the individual with the highest initial rotational stiffness, and the second represents the best trade-off solution based on a weighted

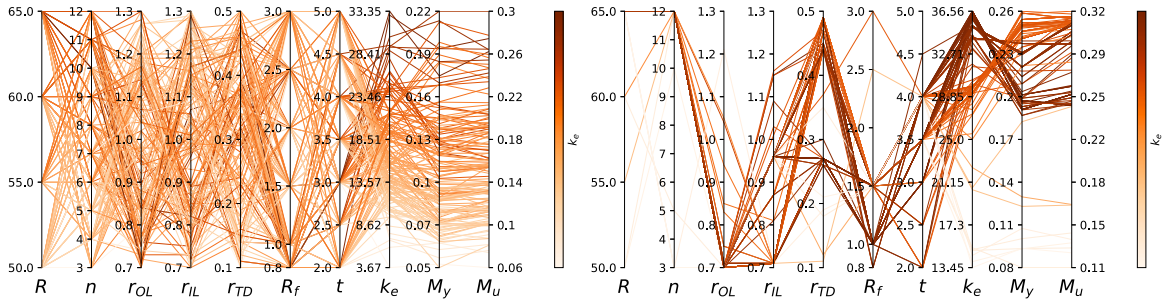

Fig. 12. KW connection with LMD.

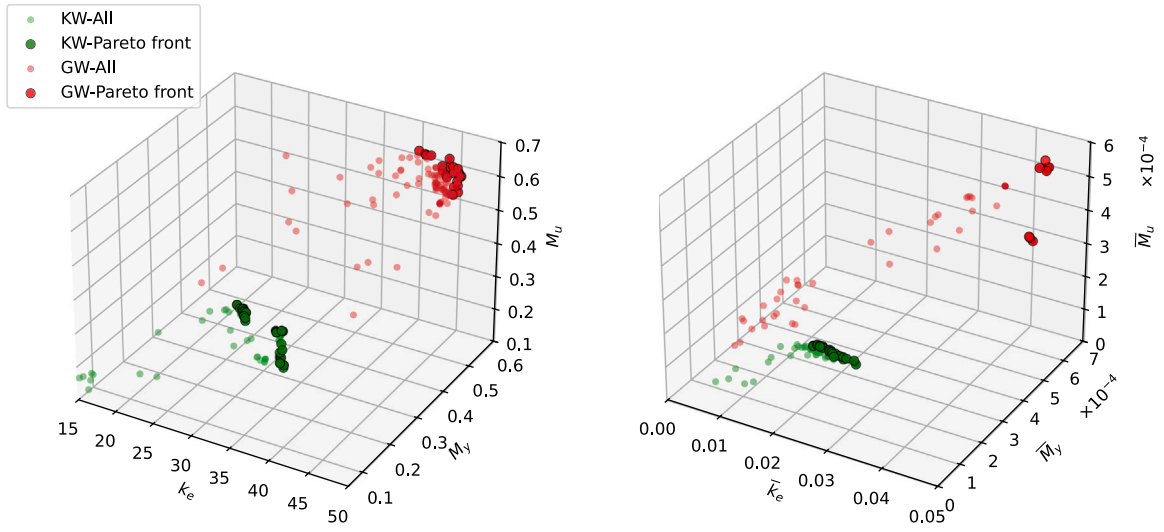

Fig. 13. Generation 150 and Pareto fronts.

objective ratio of 0.4:0.4:0.2 for (normalised) initial rotational stiffness, yield strength and peak strength, respectively. The weighted objective ratio of 0.4:0.4:0.2 considers all three objectives while maintaining a reasonable balance between initial rotational stiffness, yield strength and peak strength, thereby ensuring the acceptable performance in both elastic and inelastic stages. A wheel radius R of 65.0 mm is consistently recommended for all the connections regardless of the metal-AM processes. A tooth number n of 12 is suggested for KW connections, and between 3 and 6 for GW connections, to enhance the interlocking mechanism within the connections. KW connections tend to adopt smaller values for both the outer length ratio r_{OL} and inner length ratio r_{IL}, resulting in narrow, elongated teeth. In contrast, GW connections typically favour higher values for these parameters, leading to wider, shorter teeth. A small fillet radius R_{f} is generally recommended for all connections, except for GW connections with WAAM process, where a larger radius is adopted. A variety of thickness t are suggested for LMD-based connections, whereas the WAAM-based connections consistently adopt the minimum thickness of 2.0 mm to reduce material usage.

4.2. Explainable AI analysis

To better understand the trade-off among the initial rotational stiffness, yield strength and peak strength related to the shape parameters and highlight the feature importance, all the valid individuals from the entire optimisation process were collected. XGBoost (eXtreme Gradient Boosting) was employed subsequently to develop a machine learning model capable of capturing complex relationship among the parameters and objectives. To interpret the model, SHAP (SHapley additive exPlanations) tool was utilised. XGBoost is a sequential ensemble learning method in which each tree is trained to correct the errors of the previous one [67]. Compared to neural networks, it is often regarded as more interpretable, as it allows users to assess the relative importance of each feature. SHAP values provide insight into how each feature influences a specific prediction by computing the average marginal contribution of the feature across all possible feature combinations [68,69]. In this framework, features are conceptualised as "players" in a cooperative game, contributing to the final prediction. The magnitude and sign of the SHAP values indicate the strength and direction of each feature's effect on the model output [70]. Fig. 15 shows the SHAP values for both KW and GW connections with LMD and WAAM processes. It is noted that the objective values of yield and peak strengths of the connections with WAAM process were scaled by a factor of 10 to improve visual clarity, since the original normalised values are relatively small.

The SHAP values for KW connections with LMD process are shown in Fig. 15(a). It is clear that the wheel radius R, tooth number n and tooth depth ratio r_{TD} have the most significant influence on all three objectives, compared to the other shape parameters. Although four values of R were considered, larger wheel sizes generally provide

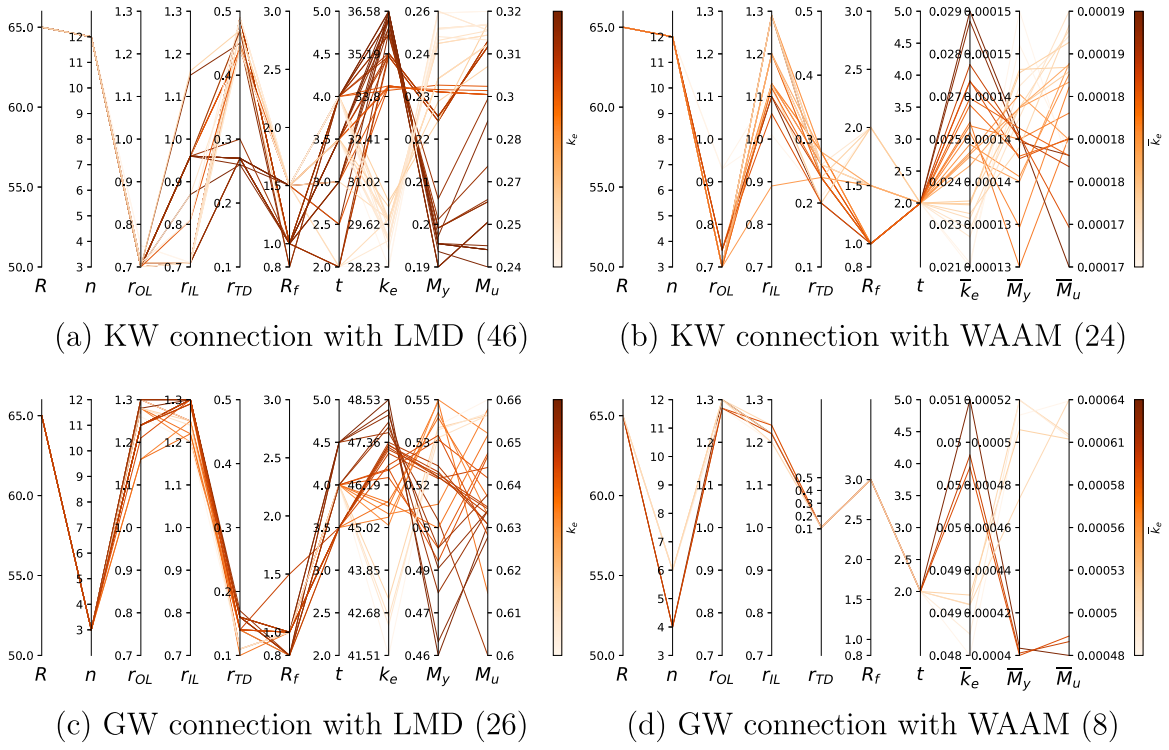

Fig. 14. Pareto fronts (generation 150).

Table 4
Optimisation results.

Connection	LMD	WAAM
KW	R: 65.0 mm; n: 12; r_{OL}: 0.70-0.75; r_{IL}: 0.71-1.16; r_{TD}: 0.26-0.49; R_f: 0.8-1.5 mm; t: 2.0-4.0 mm	R: 65.0 mm; n: 12; r_{OL}: 0.70-0.93; r_{IL}: 0.89-1.29; r_{TD}: 0.20-0.28; R_f: 1.0-2.0 mm; t: 2.0 mm
GW	R: 65.0 mm; n: 3; r_{OL}: 1.16-1.30; r_{IL}: 1.20-1.30; r_{TD}: 0.10-0.17; R_f: 0.8-1.5 mm; t: 3.5-4.5 mm	R: 65.0 mm; n: 4-6; r_{OL}: 1.28-1.30; r_{IL}: 1.20-1.24; r_{TD}: 0.11; R_f: 3.0 mm; t: 2.0 mm

higher moment-resisting capacity, regardless of the objectives of initial rotational stiffness, yield strength and peak strength, as the moment arm is longer. Accordingly, only wheels with a radius of R = 65.0 mm exhibit positive SHAP values, while all smaller radii show negative contributions. A similar trend was observed for the tooth number n, where only configurations with 11 or more teeth yield positive SHAP values. This is because the limit state of the KW connection is joist's failure, and increasing the tooth number n can boost the interlocking mechanism. The outer length ratio r_{OL} appears to have smaller influence compared to the previously discussed shape parameters. Only lower values of r_{OL}, around 0.7, yield positive SHAP values for all three objectives. Higher values of r_{OL} may lead to positive SHAP values but with limited cases. This impact is likely due to the fact that increasing the outer length reduces the height of each web segment within each interlocking part, especially as the tooth number n increases. The ratios of 0.70–0.75 are finally recommended. For the inner length ratio r_{IL}, the impact on the initial rotational stiffness appears minimal. However, a reduction in r_{IL} slightly improves both yield strength and peak strength. The tooth depth ratio r_{TD} has a significant positive effect on initial rotational stiffness up to a value of 0.3. After that, this effect gradually diminishes and remains relative constant as the tooth depth continue to increase. For yield and peak strengths, the SHAP values monotonically increase as the teeth become deeper, with positive contributions emerging after r_{TD} = 0.3. This suggests that elongated teeth generally enhance the interlocking mechanism between components, thereby improving yield

strength and peak strength. However, they may compromise the bearing behaviour during the initial loading stage, leading to a reduction in initial rotational stiffness. Smaller fillet radii R_f will increase curvature at the shape corners, which can enhance initial rotational stiffness. For yield strength, a fillet radius of approximately 1.5 mm yields better outcomes, whereas peak strength shows no significant dependence on R_f. By inspecting the histogram, it is observed that values of r_{TD} around 0.5 and $R_f \leq 1.5$ mm are more frequently selected in the population, but the corresponding SHAP values exhibit opposite signs, indicating the presence of a trade-off in their influence on the objectives. The wheel thickness t also demonstrates minimal influence on SHAP values in comparison to the aforementioned parameters. Both thicker and thinner configurations can produce favourable results across all the objectives, as illustrated in Fig. 14(a).

The SHAP values for KW connections with WAAM process are shown in Fig. 15(b). The effects of wheel radius R, tooth number n and fillet radius R_f are similar to those observed in KW-LMD connections. A shorter outer length, which increases the height of the joist segments for interlocking, enhances the normalised initial rotational stiffness. However, the outer length shows insignificant influence on normalised yield strength or peak strength. Similarly, the inner tooth length has negligible impact on all three normalised objectives. In contrast, the SHAP values for the tooth depth ratio r_{TD} increase and then decrease as the ratio rises, for all three objectives, and an optimal range of r_{TD} between 0.20 and 0.28 is recommended. This corresponds to a balanced tooth profile that is neither overly elongated nor shallow. The wheel thickness t is the most importance feature, and the minimal thickness of 2.0 mm is suggested to reduce material use. Again, values of $0.15 < r_{TD} \leq 0.3$ and $R_f \leq 2.0$ mm are more popular, but the corresponding SHAP values appear opposite signs, resulting in the trade-off in the objectives.

Fig. 15(c) shows the SHAP values for GW connections with LMD process. The effects of wheel radius R are similar to KW connections, as the larger moment arm can provide an increased moment resistance. However, the tooth number n becomes insignificant on the SHAP values for all three objectives. Larger values for both the outer and inner tooth lengths consistently improve initial rotational stiffness, yield strength and peak strength. This is due to the larger width of the teeth can increase the effective moment arm at the interlocking interface between male and female wheels, as illustrated in Fig. 2. While the tooth depth appears to be less important for either yield strength or peak strength, the shorter tooth depth can improve the interlocking mechanism and hence increase the initial rotational stiffness. The fillet radius R_f has negligible effects on all objectives. Increasing the wheel thickness t generally improves the SHAP values for all objectives, identified as the most important feature for yield strength and peak strength. By inspecting the histogram, the competing behaviour among the objectives mainly comes from n, r_{OL} and r_{TD}.

Fig. 15(d) shows the SHAP values for GW connections with WAAM process, where the use of material is restricted. The effects of the wheel parameters including wheel radius R, tooth number n, outer length ratio r_{OL}, inner length ratio r_{IL} and fillet radius of the corners R_f are similar to those observed in the GW connections with LMD process. Both the tooth depth ratio r_{TD} and the wheel thickness t are the most important features, increasing of which resulted in significantly reduced SHAP values across all three objectives. The reason is consistent with that observed in KW-WAAM connections, where smaller tooth depth and thinner wheels improve material efficiency and mechanical performance. It can be noticed that n and r_{IL} contribute to a trade-off among objectives, as indicated by the opposing signs of the SHAP values.

5. Frame level assessment

5.1. Model definition

In order to evaluate the frame-level performance, a H-frame configuration was modelled, incorporating conventional 3 × 3 screw connection with 5.4-mm-in-diameter screws, original and optimised KW and GW connections. The original model employed a standard wheel shape with $r_{OL} = 1.0$, $r_{IL} = 1.0$ for all connections. The optimised shapes were taken from the second examples in Table 4, based on the weighted objective (0.4:0.4:0.2) for (normalised) initial stiffness, yield strength and peak strength. All the wheel shape parameters are summarised in Table 5.

The setup of the FE modelling is shown in Fig. 16. This frame was derived from a six-storey building, with a centre-to-centre span of 6000 mm and a storey height of 3000 mm. Each side frame was repeated by 600 mm. The CFS channel sections used for studs and face tracks were 150M14-75 and 154M12-70, respectively. Two CFS sections, 240M13-75 and 240M16-75, were used as joists to evaluate the improvements in mechanical performance of the optimised connections. The dead and live loads applied to all floors were 1 kN/m^2 and 2 kN/m^2, respectively, according to EN 1991-1-1 [71]. Pin-end boundary conditions were applied to the reference points coupling the tops and the bottoms of studs. Lateral transitional restraints were also applied along the top edges of the joists to simulate the restraint provided by the floor sheathing. Two load cases were considered including sole gravity loading and gravity loading combined with lateral pushover targeting a lateral drift of the minimal of 80% post peak degradation or 4.0%, on the basis of the ultimate limit state. The gravity loads from the upper storeys were applied as concentrated loads at the reference points located at the top of the studs, while the gravity loads from the floor sheathing were applied as distributed area loads to the top flanges of the joists. A storey weight of 10.66 kN was also calculated based on EN 1998-1-1 [72] to normalise the base shear.

5.2. Results

Figs. 17 and 18 show the von Mises stress contour plots at the final pushover state and the deformed shapes of the joists along the normalised base shear-drift curves for all the H-frames with screw, original and optimised KW and GW connections, respectively. Table 6 summarises the analysis results, where Δ_{def} denotes the joist deflection under gravity loading, and $\bar{K}_i$, $\bar{F}_y$ and $\bar{F}_u$ are the normalised lateral initial stiffness, yield and ultimate strength under gravity loading and pushover, respectively. As shown in Fig. 17(a), the failure mode of screw connections is characterised by bearing in the joist web under lateral loading. When the joist section was upgraded from 240M13-75 to 240M16-75, the initial stiffness increased by 14.3%, while the yield and ultimate strengths remained essentially unchanged. The maximum joist deflection under gravity loading was also reduced by approximately 17.5%. In all KW connections (Figs. 17(b) and 17(c)), the joist yielding/buckling governs the limit state, while the wheel components remain elastic. The enhanced mechanical performance of the optimised connections increases the loading demands of the joists. Therefore, significant distortion buckling was observed in the KW connections with the joists of 240M13-75. This, however, was mitigated by increasing the thickness of the joist section using 240M16-75. As shown on the left side of Fig. 18(a), the maximum deflections for the H-frames with KW-LMD and KW-WAAM connections using the joist section of 240M13-75 were reduced by 19.4% and 16.5%, respectively, when optimised. Besides, as shown on the right side of Fig. 18(a), the initial stiffness, yield and peak strengths were increased by 101.2%, 212.6% and 164.7% for KW-LMD, and 103.9%, 165.6% and 151.9% for KW-WAAM connections, respectively, for the optimised connections.

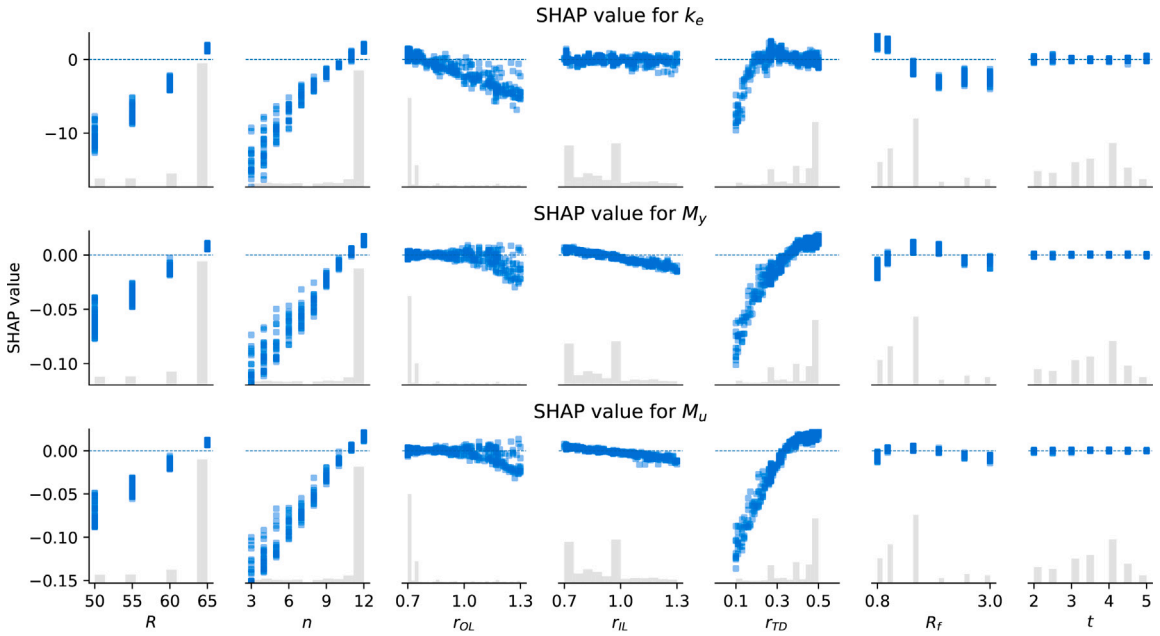

(a) KW connection with LMD process

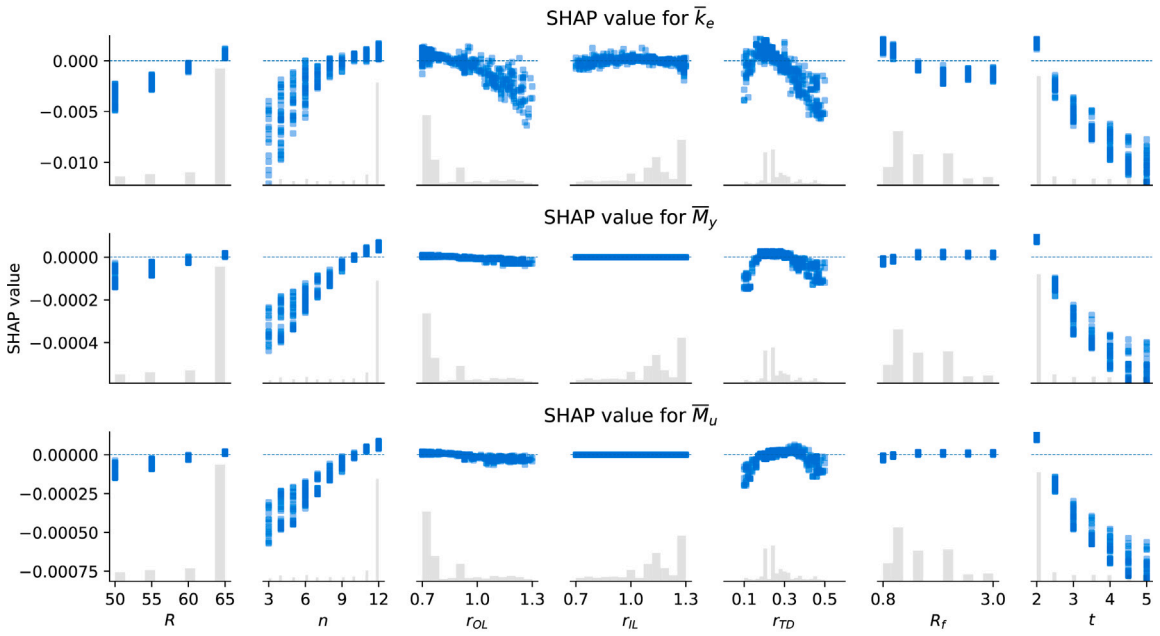

(b) KW connection with WAAM process

Fig. 15. SHAP values.

Figs. 17(d) and 17(e) show the von Mises stress plots for H-frames with GW-LMD and GW-WAAM connections at the final loading state, respectively. Similar to the KW connections, joist yielding/buckling was the governing limit state, along with limited yielding in studs. By increasing the joist thickness (240M16-75), the joist buckling effects were mitigated, while the yielding in studs slightly increased. In both cases, the female and male wheel components remained elastic, indicating that the optimised wheel components can enhance the interlocking mechanism between the female and male components and improve the efficiency of material. The maximum deflections of the joists in the H-frame with optimised GW connections using 240M13-75 joist section were 18.8% and 16.7% less than those of H-frames with original connections, as shown in the left of Fig. 18(b). Further, the normalised initial stiffness, yield strength and peak strength were increased by 74.4%, 40.5% and 41.2% for GW-LMD, and 67.4%, 17.9% and 30.3% for GW-WAAM optimised connections, respectively, compared with those of the corresponding original connections, as shown in the right of Fig. 18(b). These results confirm that both the gravity- and lateral force-resisting responses of KW and GW H-frames can be substantially improved through optimised wheel connection designs.

As shown in Table 6, by adopting optimised wheel shape, H-frames with KW connections achieve gravity- and lateral force-resisting capacities comparable to those of the screw-connected systems for both joist sections, with increases in yield and ultimate strengths of up to 57.1%

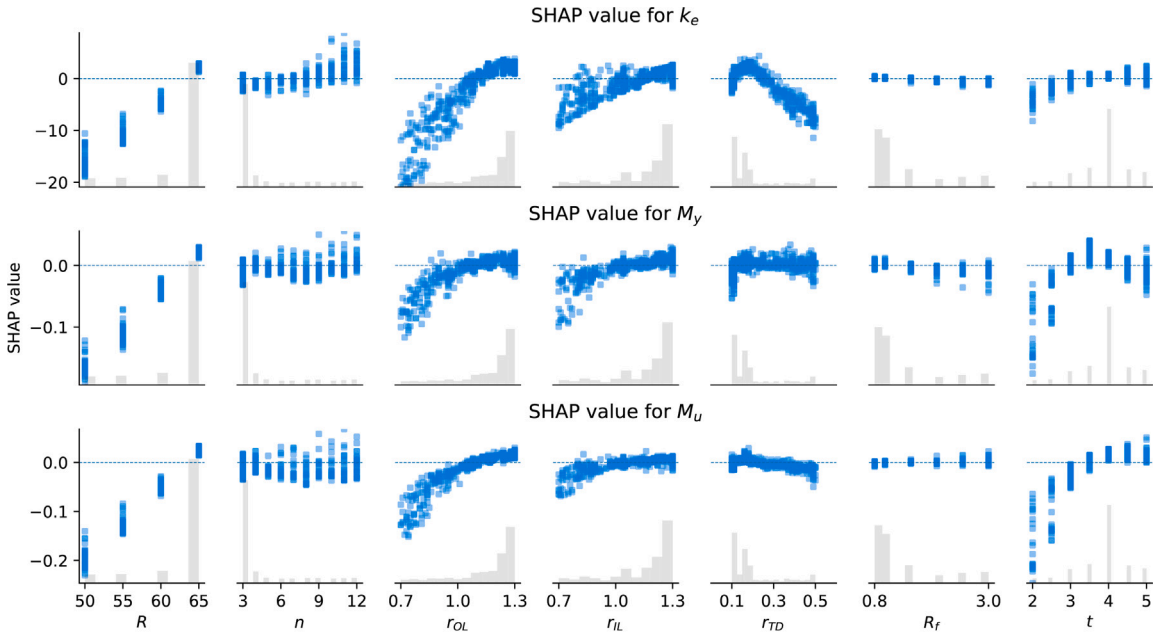

(c) GW connection with LMD process

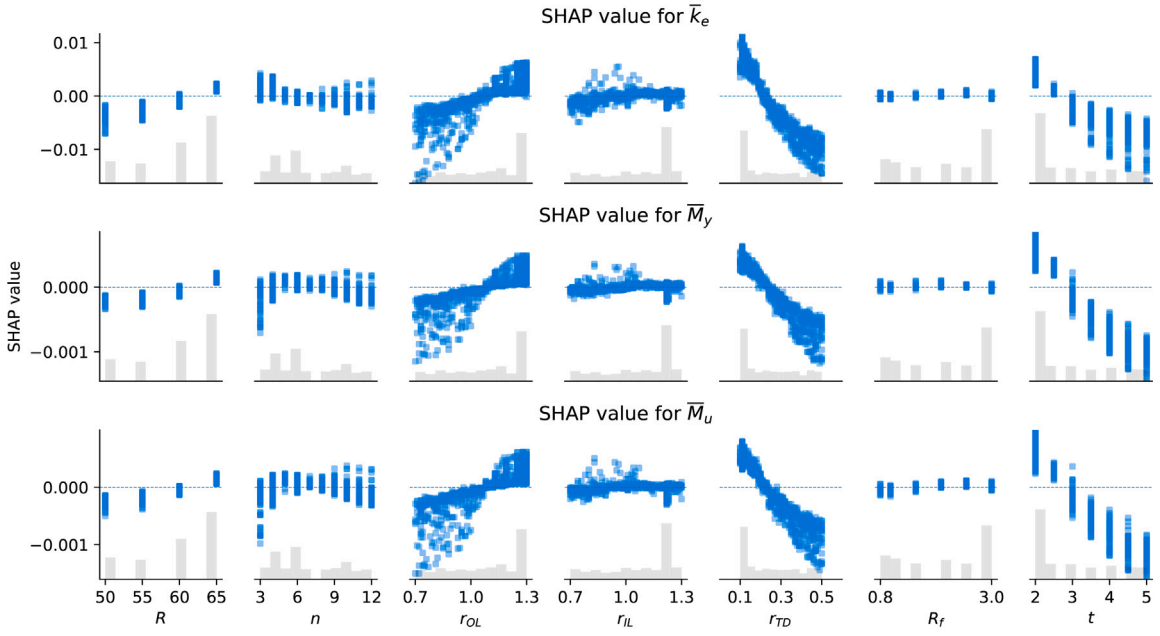

(d) GW connection with WAAM process

Fig. 15. (*continued*).

and 51.4%, respectively. More significantly, H-frames with GW connections outperformed those with screw connections, exhibiting reductions in deflection of up to 14.3% and improvements in initial stiffness, yield strength, and ultimate strength of up to 31.4%, 125.0% and 122.9%, respectively. Nevertheless, the significance of the research is mainly related to the whole-life advantages of AM connections compared with the conventional mechanical fasteners. Compared to conventional LSF systems, the AM-LSF system developed herein can potentially provide design and manufacturing flexibility, faster construction, improved quality due to reduced manual operations, and ease of dismantling and non-destructive deconstruction, which facilitates future adaptions and reuse.

5.3. Comparisons of KW and GW connections

The primary difference between the KW and GW connections lies in their interlocking mechanisms. In the KW connection, interlocking is achieved through the interaction between the wheel component and the joist web. However, due to the slenderness of the web, the bearing capacity of the web teeth after cutting are relatively low in some cases. The optimisation discussed above, actually, aims to identify the most effective tooth geometry on the web to improve moment resistance. For the GW connection, however, the interlocking is achieved by bearing interaction between female and male wheel components. In general, this configuration provides greater bearing capacity compared to the

Table 5
Parameters for optimised and original wheel shapes.

Type	Connection	Wheel parameters	Illustration
Original	All	R = 65.0 mm, n = 4, r_{OL} = 1.0, r_{IL} = 1.0, r_{TD} = 0.3, R_f = 3.0 mm, t = 2.0 mm	
Optimised	KW-LMD	R = 65.0 mm, n = 12, r_{OL} = 0.70, r_{IL} = 0.71, r_{TD} = 0.49, R_f = 1.0 mm, t = 3.5	
	KW-WAAM	R = 65.0 mm, n = 12, r_{OL} = 0.70, r_{IL} = 1.29, r_{TD} = 0.24, R_f = 1.0 mm, t = 2.0 mm	
	GW-LMD	R = 65.0 mm, n = 3, r_{OL} = 1.24, r_{IL} = 1.29, r_{TD} = 0.11, R_f = 1.0 mm, t = 4.0 mm	
	GW-WAAM	R = 65.0 mm, n = 6, r_{OL} = 1.30, r_{IL} = 1.24, r_{TD} = 0.11, R_f = 3.0 mm, t = 2.0 mm	

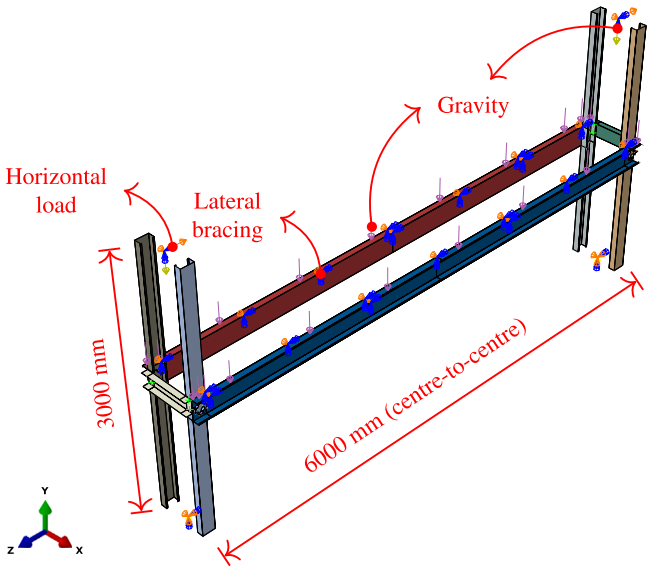

Fig. 16. H-frame finite element modelling.

Table 6
Summary.

Type	Connection	Joist section	Δ_{def} (mm)	$\bar{K}_i$	$\bar{F}_y$	$\bar{F}_u$
Screw	3 × 3/5.4 mm	240M13-75	30.32	22.52	0.29	0.34
		240M16-75	25.02	25.74	0.28	0.35
Original	KW-LMD	240M13-75	38.37	11.27	0.09	0.12
	KW-WAAM	240M13-75	38.48	10.93	0.09	0.12
	GW-LMD	240M13-75	31.99	16.98	0.32	0.37
	GW-WAAM	240M13-75	31.93	17.53	0.31	0.36
Optimised	KW-LMD	240M13-75	30.92	22.67	0.28	0.31
		240M16-75	24.17	28.37	0.44	0.53
	KW-WAAM	240M13-75	32.13	22.29	0.24	0.30
		240M16-75	24.69	28.19	0.31	0.41
	GW-LMD	240M13-75	25.98	29.60	0.45	0.52
		240M16-75	22.31	33.44	0.63	0.78
	GW-WAAM	240M13-75	26.60	29.34	0.37	0.47
		240M16-75	22.64	33.64	0.55	0.59

web-based interlocking. As such with the appropriate design of the wheel geometry, the GW connection can achieve significantly higher moment resistance. As shown in Fig. 18, the normalised initial stiffness, yield strength and peak strength were up to 30.57%, 59.33% and 65.60% higher in GW-LMD and GW-WAAM compared to KW-LMD and KW-WAAM connections, respectively. The improved performance of the GW connection, however, costs two matching wheel components, leading to increased manufacturing time, material usage and energy consumption compared to the KW connection. Further, due to the surface roughness, the WAAM process may be considered less practical for the GW connections. In contrast, the KW connection is less sensitive to the manufacturing process. Therefore, both connections present viable alternatives for construction. Each of them offers distinct advantages and trade-offs depending on performance requirements and construction constraints.

6. Conclusions

A multiple-objectives genetic algorithm optimisation framework was employed to identify the optimal wheel geometries for two types of additively manufactured key-wheel (KW) and gear-wheel (GW) connections in lightweight side framing (LSF) structures. Two metal additive manufacturing (AM) methods were considered, including laser metal deposition (LMD) and wire arc additive manufacturing (WAAM) processes. The optimised parameters included wheel radius R, tooth number n, outer length ratio r_{OL}, inner length ratio r_{IL}, tooth depth ratio r_{TD}, fillet radius of the corners R_f and wheel thickness t. The optimisation objectives were to directly maximise the initial rotational stiffness, yield strength and peak strength for the connections with LMD process, while an additional constraint was introduced by normalising these objectives with respect to material usage, in order to account for the heat input, for the connections with WAAM process. The key findings and conclusions are summarised below:

(1) The optimisation results recommend a wheel shape with 12 elongated teeth for the KW-LMD and KW-WAAM connections having tooth depth ratios r_{TD} of 0.26–0.49 and 0.20–0.28, respectively. For the GW-LMD and GW-WAAM connections, shallow-tooth wheel shapes with r_{TD} in the range of 0.10–0.17 are recommended, with n of 3 and 4–6, respectively.
(2) Trade-off behaviour was observed in both KW and GW connections regardless the AM processes. Connections achieving higher (normalised) initial rotational stiffness tend to exhibit lower yield and peak strength values, and vice versa. An explainable AI investigation reveals that the primary contributors to this trade-off are r_{TD} and R_f for both the KW-LMD and KW-WAAM connections, and n, r_{OL} and r_{TD} for the GW-LMD connection, as well as n and r_{IL} for GW-WAAM connection. Moreover, the most influential design parameters across all objectives are R, n and

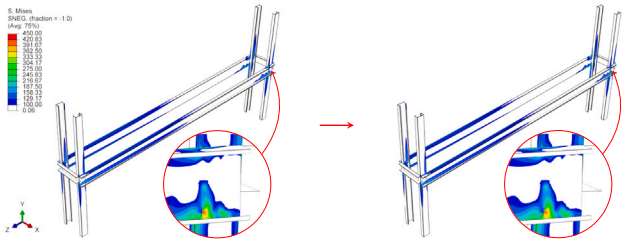

3×3-screw connection (240M13-75) 3×3-screw connection (240M16-75)

(a) 3×3-screw connections

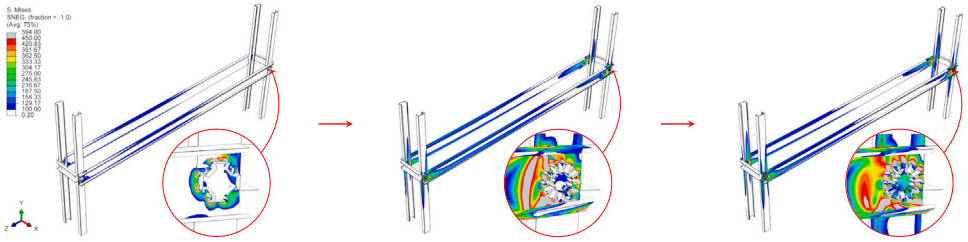

Original (240M13-75) Optimised (240M13-75) Optimised (240M16-75)

(b) KW-LMD connections

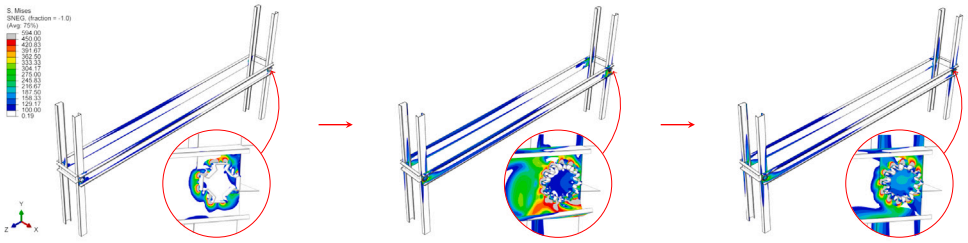

Original (240M13-75) Optimised (240M13-75) Optimised (240M16-75)

(c) KW-WAAM connections

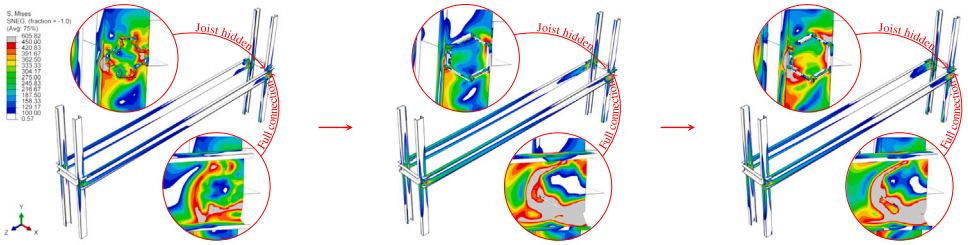

Original (240M13-75) Optimised (240M13-75) Optimised (240M16-75)

(d) GW-LMD connections

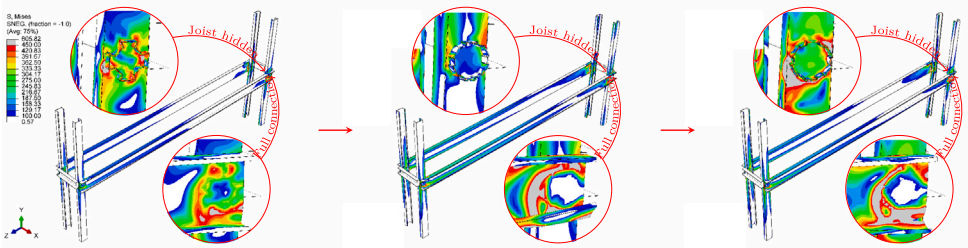

Original (240M13-75) Optimised (240M13-75) Optimised (240M16-75)

(e) GW-WAAM connections

Fig. 17. von Mises stress contour of H-frames.

r_{TD} for the KW-LMD connection, n, r_{TD} and t for the KW-WAAM connection, R, r_{OL} and t for the GW-LMD connection and r_{OL}, r_{TD} and t for the GW-WAAM connection.

(3) A frame-level ultimate limit state analysis shows that the implementation of optimised KW and GW connections can lead to notable improvements compared with the original AM-CFS

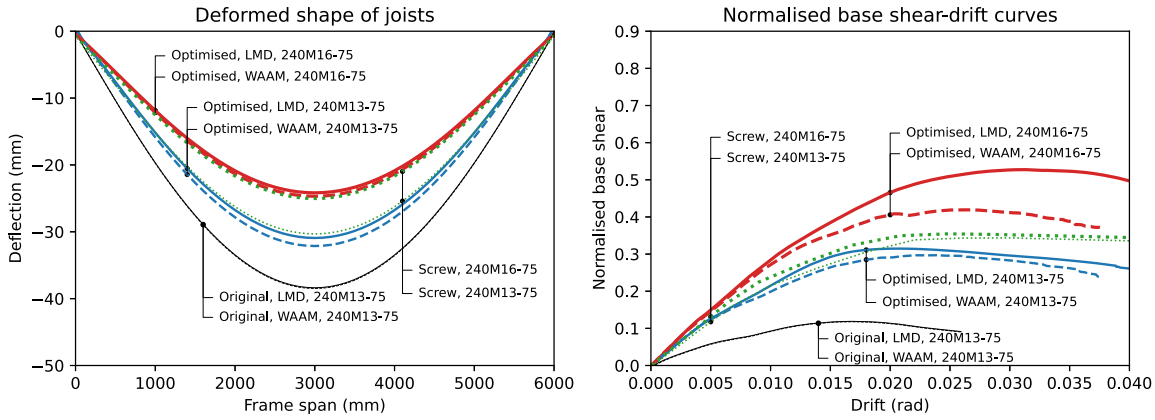

(a) H-frames with KW connections

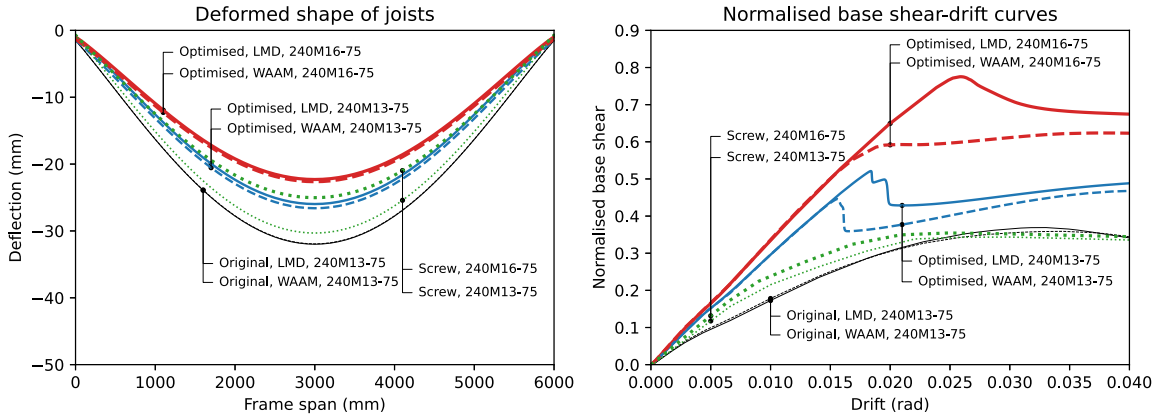

(b) H-frames with GW connections

Fig. 18. H-frame assessment.

and conventional screw connections. The maximum joist deflections are reduced by up to 19.4%, while the normalised initial stiffness, yield strength and peak strength of the frames are increased by 74.4%–112.1%, 40.5%–212.6% and 41.2%–164.7%, respectively.

(4) GW connection shows superior performance compared to the KW connection in terms of initial rotational stiffness, yield strength and peak strength. However, both connection types offer viable alternatives since each of them shows trade-offs depending on performance requirements and manufacturing practicality.

Through optimisation and explainable-AI techniques, this study sheds light on the inherent trade-offs among wheel-shape parameters and proposes optimised AM-CFS connections through validated finite element (FE) method, which can serve as a foundation for future studies. Although prototyping and experimental testing have confirmed the feasibility and efficiency of these innovative connections, metallurgical-scale details of both the substrate and the printed components remain insufficiently understood due to the influences of thermal input, cooling methods and fixturing conditions. In addition, printing quality issues, such as surface roughness, distortion and assembly clearance control, remain key challenges. Comprehensive experimental programmes and advanced numerical investigations are therefore necessary to further validate the practicality of these connections, and these aspects will be the main focus of future research.

CRediT authorship contribution statement

Chuandong Xie: Writing – original draft, Visualization, Validation, Software, Methodology, Investigation, Formal analysis, Data curation, Conceptualization. **Alireza Bagheri Sabbagh:** Writing – review & editing, Supervision, Project administration, Investigation, Conceptualization. **Ehsan Bakhshivand:** Writing – review & editing, Validation, Software, Investigation, Formal analysis. **Ornella Iuorio:** Writing – review & editing, Supervision, Project administration, Investigation, Conceptualization.

Financial disclosure

None reported.

Declaration of competing interest

The authors declare that they have no known competing financial interests or personal relationships that could have appeared to influence the work reported in this paper.

Acknowledgements

The connection developed in this paper is part of a filed patent application numbered 102025000010515 on 09 May 2025. The authors would like to thank Prof. Barbara Previtali and her team for their support through extensive prototyping and 3D printing at AS.Lab and AddMe.Lab in Politecnico di Milano. The structural tests were carried

out at the Material Testing Laboratory (LPM) of Politecnico di Milano which is much appreciated. The first and second authors acknowledge support from Engineering and Physical Sciences Research Council, the United Kingdom (EPSRC, EP/W026376/1).

Data availability

Data will be made available on request.

References

[1] Y. Dai, K. Roy, Z. Fang, G.M. Raftery, K. Ghosh, J.B.P. Lim, A critical review of cold-formed built-up members: Developments, challenges, and future directions, J. Build. Eng. 76 (2023) 107255, http://dx.doi.org/10.1016/j.jobe.2023.107255.

[2] N. Jafarifar, A. Bagheri Sabbagh, I. Uchehara, Rubberised concrete confined with thin-walled steel profiles; a ductile composite for building structures, Structures 49 (2023) 983–994, http://dx.doi.org/10.1016/j.istruc.2023.01.134.

[3] D. Ayhan, B. Schafer, Cold-formed steel ledger-framed construction floor-to-wall connection behavior and strength, J. Constr. Steel Res. 156 (2019) 215–226, http://dx.doi.org/10.1016/j.jcsr.2019.01.021.

[4] H. Castaneda, K.D. Peterman, Moment-rotation response of cold-formed steel joist-to-ledger connections with variable-finishes in ledger-framed construction, J. Constr. Steel Res. 176 (2021) 106396, http://dx.doi.org/10.1016/j.jcsr.2020.106396.

[5] A. Bagheri Sabbagh, S. Torabian, Semi-rigid floor-to-wall connections using side-framed lightweight steel structures: Concept development, Thin-Walled Struct. 160 (2021) 107345, http://dx.doi.org/10.1016/j.tws.2020.107345.

[6] C. Buchanan, L. Gardner, Metal 3D printing in construction: A review of methods, research, applications, opportunities and challenges, Eng. Struct. 180 (2019) 332–348, http://dx.doi.org/10.1016/j.engstruct.2018.11.045.

[7] A. Altamirano-Gamiño, L.E. Reyes-Gordillo, F. Reyes-Calderón, H.J. Vergara-Hernández, V. García-García, Three-dimensional metal printing of inclined walls and conic geometries through a WAAM system with optimized mobility and torch control: Metallographic and mechanical characterization, Int. J. Adv. Manuf. Technol. 137 (2025) 5863–5876, http://dx.doi.org/10.1007/s00170-025-15525-8.

[8] P. Kyvelou, H. Slack, D. Daskalaki Mountanou, M.A. Wadee, T.B. Britton, C. Buchanan, L. Gardner, Mechanical and microstructural testing of wire and arc additively manufactured sheet material, Mater. Des. 192 (2020) 108675, http://dx.doi.org/10.1016/j.matdes.2020.108675.

[9] F. Raspall, S. Araya, M. Pazols, E. Valenzuela, M. Castillo, P. Benavides, Wire arc additive manufacturing for widespread architectural application: A review informed by large-scale prototypes, Buildings 15 (2025) 906, http://dx.doi.org/10.3390/buildings15060906.

[10] Y.N. Saleh, S.A. Mourad, H.G. Salem, A.M. Ibrahim, Residual stress and distortion analysis in WAAM steel blocks: A comparative study of build strategies, Structures 75 (2025) 108798, http://dx.doi.org/10.1016/j.istruc.2025.108798.

[11] J.I. Arrizubieta, S. Martínez, A. Lamikiz, E. Ukar, K. Arntz, F. Klocke, Instantaneous powder flux regulation system for laser metal deposition, J. Manuf. Process. 29 (2017) 242–251, http://dx.doi.org/10.1016/j.jmapro.2017.07.018.

[12] B. Graf, A. Marko, T. Petrat, A. Gumenyuk, M. Rethmeier, 3D laser metal deposition: Process steps for additive manufacturing, Weld. World 62 (2018) 877–883, http://dx.doi.org/10.1007/s40194-018-0590-x.

[13] T.A. Rodrigues, V. Duarte, R.M. Miranda, T.G. Santos, J.P. Oliveira, Current status and perspectives on wire and arc additive manufacturing (WAAM), Materials 12 (2019) 1121, http://dx.doi.org/10.3390/ma12071121.

[14] L. Gardner, Metal additive manufacturing in structural engineering – review, advances, opportunities and outlook, Structures 47 (2023) 2178–2193, http://dx.doi.org/10.1016/j.istruc.2022.12.039.

[15] H. Pant, A. Arora, G.S. Gopakumar, U. Chadha, A. Saeidi, A.E. Patterson, Applications of wire arc additive manufacturing (WAAM) for aerospace component manufacturing, Int. J. Adv. Manuf. Technol. 127 (2023) 4995–5011, http://dx.doi.org/10.1007/s00170-023-11623-7.

[16] A. Zocca, J. Lüchtenborg, T. Mühler, J. Wilbig, G. Mohr, T. Villatte, F. Léonard, G. Nolze, M. Sparenberg, J. Melcher, K. Hilgenberg, J. Günster, Enabling the 3D printing of metal components in μ -gravity, Adv. Mater. Technol. 4 (2019) 1900506, http://dx.doi.org/10.1002/admt.201900506.

[17] J. Ni, H. Ling, S. Zhang, Z. Wang, Z. Peng, C. Benyshek, R. Zan, A.K. Miri, Z. Li, X. Zhang, J. Lee, K.J. Lee, H.J. Kim, P. Tebon, T. Hoffman, M.R. Dokmeci, N. Ashammakhi, X. Li, A. Khademhosseini, Three-dimensional printing of metals for biomedical applications, Mater. Today Bio 3 (2019) 100024, http://dx.doi.org/10.1016/j.mtbio.2019.100024.

[18] A. Gasser, G. Backes, I. Kelbassa, A. Weisheit, K. Wissenbach, Laser additive manufacturing: Laser metal deposition (LMD) and selective laser melting (SLM) in turbo-engine applications, Laser Tech. J. 7 (2010) 58–63, http://dx.doi.org/10.1002/latj.201090029.

[19] A.H. Alami, A. Ghani Olabi, A. Alashkar, S. Alasad, H. Aljaghoub, H. Rezk, M.A. Abdelkareem, Additive manufacturing in the aerospace and automotive industries: Recent trends and role in achieving sustainable development goals, Ain Shams Eng. J. 14 (2023) 102516, http://dx.doi.org/10.1016/j.asej.2023.102516.

[20] A. Taşdemir, S. Nohut, An overview of wire arc additive manufacturing (WAAM) in shipbuilding industry, Ships Offshore Struct. 16 (2021) 797–814, http://dx.doi.org/10.1080/17445302.2020.1786232.

[21] G. Ambrogio, F. Gagliardi, M. Muzzupappa, L. Filice, Additive-incremental forming hybrid manufacturing technique to improve customised part performance, J. Manuf. Process. 37 (2019) 386–391, http://dx.doi.org/10.1016/j.jmapro.2018.12.008.

[22] M.H. Baqershahi, C. Ayas, E. Ghafoori, Design optimisation for hybrid metal additive manufacturing for sustainable construction, Eng. Struct. 301 (2024) 117355, http://dx.doi.org/10.1016/j.engstruct.2023.117355.

[23] X. Meng, L. Gardner, Hybrid construction featuring wire arc additive manufacturing: Review, concepts, challenges and opportunities, Eng. Struct. 326 (2025) 119337, http://dx.doi.org/10.1016/j.engstruct.2024.119337.

[24] H. Kloft, L.P. Schmitz, C. Müller, V. Laghi, N. Babovic, A. Baghdadi, Experimental application of robotic wire-and-arc additive manufacturing technique for strengthening the I-Beam profiles, Buildings 13 (2023) 366, http://dx.doi.org/10.3390/buildings13020366.

[25] L. Gardner, J. Li, X. Meng, C. Huang, P. Kyvelou, I-section steel columns strengthened by wire arc additive manufacturing - concept and experiments, Eng. Struct. 306 (2024) 117763, http://dx.doi.org/10.1016/j.engstruct.2024.117763.

[26] P. Kyvelou, C. Huang, J. Li, L. Gardner, Residual stresses in steel I-sections strengthened by wire arc additive manufacturing, Structures 60 (2024) 105828, http://dx.doi.org/10.1016/j.istruc.2023.105828.

[27] J. Yang, M.A. Wadee, L. Gardner, Strengthening of steel I-section beams by wire arc additive manufacturing — Concept and experiments, Eng. Struct. 322 (2025) 119113, http://dx.doi.org/10.1016/j.engstruct.2024.119113.

[28] A. Kanyilmaz, F. Berto, I. Paoletti, R.J. Caringal, S. Mora, Nature-inspired optimization of tubular joints for metal 3D printing, Struct. Multidiscip. Optim. 63 (2021) 767–787, http://dx.doi.org/10.1007/s00158-020-02729-7.

[29] V. Laghi, N. Babovic, E. Benvenuti, H. Kloft, Blended structural optimization of steel joints for wire-and-arc additive manufacturing, Eng. Struct. 300 (2024) 117141, http://dx.doi.org/10.1016/j.engstruct.2023.117141.

[30] B. Gil, R. Goñi, M. Fábregas, E. Bayo, Design and testing of steel additive-manufactured moment-resistant beam-to-column connection, J. Constr. Steel Res. 219 (2024) 108747, http://dx.doi.org/10.1016/j.jcsr.2024.108747.

[31] K. Monteiro, C. Zhu, A.F. Santos, L.S. da Silva, T. Tankova, Integrated topological optimization and production of an additively manufactured steel T-joint: A case study, Structures 74 (2025) 108511, http://dx.doi.org/10.1016/j.istruc.2025.108511.

[32] E. Ghafoori, H. Dahaghin, C. Diao, N. Pichler, L. Li, M. Mohri, J. Ding, S. Ganguly, S. Williams, Fatigue strengthening of damaged steel members using wire arc additive manufacturing, Eng. Struct. 284 (2023) 115911, http://dx.doi.org/10.1016/j.engstruct.2023.115911.

[33] H. Dahaghin, M. Motavalli, H. Moshayedi, S.M. Zahrai, E. Ghafoori, Wire and arc additive manufacturing for strengthening of metallic components, Thin-Walled Struct. 203 (2024) 112074, http://dx.doi.org/10.1016/j.tws.2024.112074.

[34] Y. Wu, J. Fang, C. Wu, C. Li, G. Sun, Q. Li, Additively manufactured materials and structures: A state-of-the-art review on their mechanical characteristics and energy absorption, Int. J. Mech. Sci. 246 (2023) 108102, http://dx.doi.org/10.1016/j.ijmecsci.2023.108102.

[35] J. McCall, Genetic algorithms for modelling and optimisation, J. Comput. Appl. Math. 184 (2005) 205–222, http://dx.doi.org/10.1016/j.cam.2004.07.034.

[36] S. Sivanandam, S. Deepa, Introduction To Genetic Algorithms, Springer Berlin Heidelberg, Berlin, Heidelberg, 2008, http://dx.doi.org/10.1007/978-3-540-73190-0.

[37] D. Huang, S. Pei, A. Busch, Optimizing displacement-based seismic design of mass timber rocking walls using genetic algorithm, Eng. Struct. 229 (2021) 111603, http://dx.doi.org/10.1016/j.engstruct.2020.111603.

[38] S. Hu, X. Lei, Machine learning and genetic algorithm-based framework for the life-cycle cost-based optimal design of self-centering building structures, J. Build. Eng. 78 (2023) 107671, http://dx.doi.org/10.1016/j.jobe.2023.107671.

[39] J. Lee, S.-M. Kim, H. Seon Park, Optimum design of cold-formed steel columns by using micro genetic algorithms, Thin-Walled Struct. 44 (2006) 952–960, http://dx.doi.org/10.1016/j.tws.2006.08.021.

[40] D.T. Phan, J.B.P. Lim, T.T. Tanyimboh, A.M. Wrzesien, W. Sha, R.M. Lawson, Optimal design of cold-formed steel portal frames for stressed-skin action using genetic algorithm, Eng. Struct. 93 (2015) 36–49, http://dx.doi.org/10.1016/j.engstruct.2015.02.037.

[41] H. Parastesh, I. Hajirasouliha, H. Taji, A. Bagheri Sabbagh, Shape optimization of cold-formed steel beam-columns with practical and manufacturing constraints, J. Constr. Steel Res. 155 (2019) 249–259, http://dx.doi.org/10.1016/j.jcsr.2018.12.031.

[42] Y. Dai, Z. Fang, K. Roy, G.M. Raftery, J.B.P. Lim, Optimal design of cold-formed steel face-to-face built-up columns through deep belief network and genetic algorithm, Structures 56 (2023) 104906, http://dx.doi.org/10.1016/j.istruc.2023.104906.

[43] A.M. Salih, Explainable artificial intelligence and multicollinearity : A mini review of current approaches, 2024, http://dx.doi.org/10.48550/arXiv.2406.11524, arXiv:2406.11524.
[44] A.K. Gizzini, Y. Medjahdi, A.J. Ghandour, L. Clavier, Explainable AI for enhancing efficiency of DL-based channel estimation, 2024, arXiv:2407.07009.
[45] X. Wen, R.O. Weber, A. Sen, D. Hannan, S.C. Nesbit, V. Chan, A. Goffi, M. Morris, J.C. Hunninghake, N.E. Villalobos, E. Kim, C.J. MacLellan, The impact of an XAI-augmented approach on binary classification with scarce data, 2024, http://dx.doi.org/10.48550/arXiv.2407.06206, arXiv:2407.06206.
[46] C. Xie, J. Hu, G. Vasdravellis, X. Wang, S. Cheng, Explainable AI model for predicting equivalent viscous damping in dual frame-wall resilient system, J. Build. Eng. (2024) 110564, http://dx.doi.org/10.1016/j.jobe.2024.110564.
[47] F. Guaglione, A.A. Benni, B. Previtali, Exploring wire laser metal deposition of 316L stainless steel as a viable solution for combined manufacturing routes, Prog. Addit. Manuf. 10 (2025) 3859–3878, http://dx.doi.org/10.1007/s40964-024-00832-5.
[48] A. Spinasa, B. Weber, X. Meng, R. Zhang, M. Nitawaki, L. Gardner, Influence of process parameters on the physical and material properties of WAAM steels, Constr. Build. Mater. 479 (2025) 141078, http://dx.doi.org/10.1016/j.conbuildmat.2025.141078.
[49] B. Weber, X. Meng, L. Gardner, Optimised and 3D printed steel garden bridge: From design to experimental verification, Autom. Constr. 181 (2026) 106638, http://dx.doi.org/10.1016/j.autcon.2025.106638.
[50] M. Megahed, H.-W. Mindt, N. N'Dri, H. Duan, O. Desmaison, Metal additive-manufacturing process and residual stress modeling, Integr. Mater. Manuf. Innov. 5 (2016) 61–93, http://dx.doi.org/10.1186/s40192-016-0047-2.
[51] M. Biegler, B. Graf, M. Rethmeier, In-situ distortions in LMD additive manufacturing walls can be measured with digital image correlation and predicted using numerical simulations, Addit. Manuf. 20 (2018) 101–110, http://dx.doi.org/10.1016/j.addma.2017.12.007.
[52] W. Ji, O. Muransky, C. Barr, R. Subbaramaiah, N.J. Edwards, M. Brandt, S. Palanisamy, C. Wallbrink, Development and experimental validation of a thermo-metallurgical-mechanical model of the laser metal deposition (LMD) process, Int. J. Press. Vessels Pip. 211 (2024) 105261, http://dx.doi.org/10.1016/j.ijpvp.2024.105261.
[53] J. Park, J. y. Kim, I. Ji, S.H. Lee, Numerical and experimental investigations of laser metal deposition (LMD) using STS 316L, Appl. Sci. 10 (2020) 4874, http://dx.doi.org/10.3390/app10144874.
[54] ASCE, Seismic evaluation and retrofit of existing buildings (ASCE/SEI 41-23), 2023, http://dx.doi.org/10.1061/9780784416112.
[55] Z. Chen, L. Yuan, Z. Pan, H. Zhu, N. Ma, D. Ding, H. Li, A comprehensive review and future perspectives of simulation approaches in wire arc additive manufacturing (WAAM), Int. J. Extrem. Manuf. 7 (2025) 022016, http://dx.doi.org/10.1088/2631-7990/ada099.
[56] F.-A. Fortin, F.-M. De Rainville, M.-A. Gardner, M. Parizeau, C. Gagné, DEAP: Evolutionary algorithms made easy, J. Mach. Learn. Res. 13 (2012) 2171–2175.
[57] FreeCAD Community, FreeCAD: Your own 3D parametric modeler, 2025.
[58] Dassault Systèmes Simulia Corp, Abaqus 2024, 2024.
[59] Python Software Foundation, The python language reference, 2025, https://docs.python.org/3/reference/index.html.
[60] K. Deb, H. Jain, An evolutionary many-objective optimization algorithm using reference-point-based nondominated sorting approach, part I: Solving problems with box constraints, IEEE Trans. Evol. Comput. 18 (2014) 577–601, http://dx.doi.org/10.1109/TEVC.2013.2281535.
[61] Eurocode, Eurocode 3. Design of steel structures - general rules and rules for buildings (EN 1993-1-1), 2023.
[62] L. Gardner, X. Yun, Description of stress-strain curves for cold-formed steels, Constr. Build. Mater. 189 (2018) 527–538, http://dx.doi.org/10.1016/j.conbuildmat.2018.08.195.
[63] P. Hradil, A. Talja, E. Real, E. Mirambell, B. Rossi, Generalized multistage mechanical model for nonlinear metallic materials, Thin-Walled Struct. 63 (2013) 63–69, http://dx.doi.org/10.1016/j.tws.2012.10.006.
[64] S. Cacace, V. Furlan, R. Sorci, Q. Semeraro, M. Boccadoro, Using recycled material to produce gas-atomized metal powders for additive manufacturing processes, J. Clean. Prod. 268 (2020) 122218, http://dx.doi.org/10.1016/j.jclepro.2020.122218.
[65] C. Huang, P. Kyvelou, L. Gardner, Stress-strain curves for wire arc additively manufactured steels, Eng. Struct. 279 (2023) 115628, http://dx.doi.org/10.1016/j.engstruct.2023.115628.
[66] P. Kyvelou, C. Buchanan, L. Gardner, Numerical simulation and evaluation of the world's first metal additively manufactured bridge, Structures 42 (2022) 405–416, http://dx.doi.org/10.1016/j.istruc.2022.06.012.
[67] D. Elavarasan, D.R. Vincent, Reinforced XGBoost machine learning model for sustainable intelligent agrarian applications, J. Intell. Fuzzy Systems 39 (2020) 7605–7620, http://dx.doi.org/10.3233/JIFS-200862.
[68] K. Lin, Y. Gao, Model interpretability of financial fraud detection by group SHAP, Expert Syst. Appl. 210 (2022) 118354, http://dx.doi.org/10.1016/j.eswa.2022.118354.
[69] M.L. Martini, S.N. Neifert, E.K. Oermann, J.T. Gilligan, R.J. Rothrock, F.J. Yuk, J.S. Gal, D.A. Nistal, J.M. Caridi, Application of cooperative game theory principles to interpret machine learning models of nonhome discharge following spine surgery, Spine 46 (2021) 803, http://dx.doi.org/10.1097/BRS.0000000000003910.
[70] R. Stirnberg, J. Cermak, S. Kotthaus, M. Haeffelin, H. Andersen, J. Fuchs, M. Kim, J.-E. Petit, O. Favez, Meteorology-driven variability of air pollution (PM_1) revealed with explainable machine learning, Atmos. Chem. Phys. 21 (2021) 3919–3948, http://dx.doi.org/10.5194/acp-21-3919-2021.
[71] Eurocode, Eurocode 1. Actions on structures - general actions - densities, self-weight, imposed loads for buildings (EN 1991-1-1), 2002.
[72] Eurocode, Eurocode 8: Design of structures for earthquake resistance – part 1: General rules, seismic actions and rules for buildings (EN1998-1-1), 2013.